Materials Advances

ROYAL SOCIETY OF CHEMISTRY

PAPER

View Article Online
View Journal | View Issue

Check for updates

Cite this: *Mater. Adv.*, 2020, **1**, 2804

The synthesis of a $Cu_{0.8}Zn_{0.2}Sb_2$–polyacrylamide nanocomposite by frontal polymerization for moisture and photodetection performance

Priyanka Chaudhary, [a] Dheeraj Kumar Maurya,[b] Ravi Kant Tripathi,[a] B. C. Yadav, *[a] Nina D. Golubeva,[c] Evgeniya I. Knerelman,[c] Igor E. Uflyand [d] and Gulzhian I. Dzhardimalieva[c]

Received 8th June 2020,
Accepted 22nd September 2020

DOI: 10.1039/d0ma00389a

rsc.li/materials-advances

Herein, the preparation of a $Cu_{0.8}Zn_{0.2}Sb_2$AAm–polymer nanocomposite synthesized *via* a frontal polymerization technique is reported, together with its humidity sensing and photoconductive behaviour. The surface texture was examined using scanning electron microscopy (SEM) analysis. X-ray diffraction (XRD) and transmission electron microscopy (TEM) studies confirm the crystallinity of the as-fabricated nanocomposite thin film based sensing element. The surface area, particle size, optical absorbance, and thermal stability of the as-fabricated thin film were successively investigated using Brunauer–Emmett–Teller (BET) analysis, particle size analysis, ultra-violet absorption studies, Fourier-transform infrared (FTIR) spectroscopy, thermogravimetric analysis (TGA), X-ray photoelectron spectroscopy (XPS), and differential scanning calorimetric (DSC) analysis. The humidity sensing characteristics were also investigated based on the capacitive performance of $Cu_{0.8}Zn_{0.2}Sb_2$AAm film when exposed to moisture. The average sensitivity (*S*) of the as-fabricated sensor was found to be ~168.477 pF/% RH at an optimum frequency of 20 Hz. The sensor exhibited rapid response and recovery times of 4.6 s and 5.6 s, respectively, with persistent stability of 96% after 60 d. Thus, the $Cu_{0.8}Zn_{0.2}Sb_2$AAm polymer-based capacitive humidity sensor shows its potential for reliable and safe use in the detection of humidity levels, as well as for photoconduction.

1. Introduction

The polymer structure of polyacrylamide (PAam) is just like a polyethylene chain with an amide group attached at one end. The PAam is synthesized by polymerization of acrylamide (AAm, C_3H_5NO), a compound obtained by the hydration of acrylonitrile. The dissolved monomers (AAm) are induced to polymerize by the action of free-radical initiators. The highly reactive amide (NH_2) group and the polymer can be chemically modified to produce a positively charged cationic polymer or a negatively charged anionic polymer.[1–3] Ionic polymers are especially useful in separating metals from residues in various mineral-processing and metallurgical operations. Because of its flocculating nature, PAam is a globally used synthetic polymer in different applications such as removal of toxic ions during water treatment, in the paper making industry, in the petroleum sector, for soil conditioning and so.[4–7]

The energy of these PAams becomes more prominent with the development of a metal–polymer complexes. The rapid development of metal incorporated polymer complexes revived the modern polymer industry by producing more advanced materials. The complexion of metal ions with polymeric ligands drastically affects the properties of the parent polymer.[8] From the technological point of view, the thermal stability of polymers is important in their high-temperature applications. Insertion of metal ions in the polymer matrix generates many charge carrier ions, thus increasing the rigidity of the polymer chains and raising the glass transition temperature (T_g) of the material. Metal-doped PAam is extensively harvested in the water-soluble polymer synthesis. Different metal–polymer complexes have been successfully synthesized by doping of transition metal ions with a divalent nature such as Cd^{2+}, Co^{2+}, Cu^{2+}, Fe^{2+}, Mn^{2+}, Ni^{2+}, and Zn^{2+} resulting in them possessing better chemical and thermal stabilities.[9–12] These metallopolymers have the functionality of polymers as well as

[a] *Nanomaterials and Sensors Research Laboratory, Department of Physics, Babasaheb Bhimrao Ambedkar University, Lucknow 226025, UP, India. E-mail: balchandra_yadav@rediffmail.com; Tel: +91 9450094590*
[b] *Electro-Materials Research Laboratory, Centre for Nanoscience and Technology, Pondicherry University, Puducherry 605014, India*
[c] *Laboratory of Metallopolymers, Institute of Problems of Chemical Physics, Russian Academy of Sciences, Chernogolovka, Moscow Region 142432, Russia*
[d] *Department of Chemistry, Southern Federal University, B. Sadovaya Str. 105/42, Rostov-on-Don, 344006, Russian Federation*

metals enabling their use to be possible in various industries such as memory devices, humidity sensors, gas sensors, solar appliances, and light-emitting devices. Depending on the precursors, different methods of production of metallopolymers (metal-containing polymers) have been reported. The preparation method proceeds in three steps:

• firstly, the interaction of the metal compound (MXn) with functionalized polymers, which means carboxyl-containing polymers, and an analogous transformation, defined as occurring when the main polymer chain remains untouched by the metal compound;

• secondly, polycondensation of the appropriate precursors occurs, when the metal ions are combined into and removed from the main chain of the polymers;

• finally, a new method, recently developed for the polymerization and copolymerization of metallopolymer monomers (metal-containing) is used. Metallopolymers are based on transition metals, and are obtained by the previously described methods.

Recently, a single metal-based polymer complex has been harvested for use in humidity sensing *via* an electrical mode as well as an optoelectronic mode.[13] Several charge carriers are a crucial factor in determining the sensing characteristic of a material.[11,13] Allocation of isovalent dopant ions in the metal sites strengthens the synergistic effect between metal ions and the host polymer.

The zinc–antimony (Zn–Sb) binary system is one of the best thermoelectric materials due to its low lattice thermal conductivity which is stable at intermediate temperatures.[14,15] This alloy contains a higher degree of atomic disorder within the whole concentration. Doping of Cu in the Zn–Sb alloys enhances the whole concentration, and leads to the higher carrier concentration. In addition, the atomic radius of Cu is compatible with the Zn–Sb polymorph and can easily be accommodated in the interstitial gaps in the Zn–Sb lattice, thus facilitating disruption in the lattice stability and reduction of the lattice thermal conductivity.[14,16,17] The Cu–Zn–Sb based ternary system fulfils the goals of technological as well as humidity sensing needs. The incorporation of this ternary system in the polymer matrix will improve thermal properties as well as providing a better sensing capability for use as a humidity sensor.

For the detection and control of humidity, large numbers of materials have been reported. These materials also play an important role in environmental monitoring for atmosphere, seed storage, agriculture, in the chemical field, in biomedical sectors, in electronics processing, and the food industry, as well as being used in daily life, for example as air conditioners and in hospitals, and so on.[18–20] A large number of sensing materials have been exploited for humidity sensing and these are mainly organic polymers, metal oxides, polymer/inorganic nanohybrids and polymer electrolytes (polyelectrolytes), and every material has its own inherent property responsible for humidity adsorption and desorption.[21–25] Nowadays the photodetection properties are also thoroughly investigated together with the humidity sensing behaviour.[26–29] Some of the nanomaterials show the extraordinary behaviour of responding to both humidity as well as acting as a photodetector. In recent years to minimize the wastage of energy and improve the energy-saving practices, photoconduction has been studied for different nanomaterials.[26,28,30] The results of a literature survey based on other metal oxides used as humidity sensors is shown in Table 1:[31–38]

Here, in the method described in the present manuscript, a ternary metal-doped AAm composite was used for photoconduction behaviour and as a humidity sensor for the measurement of moisture. Previous investigations were focussed only on single metal-doped complexes but here a stable ternary system for humidity sensing is reported for the first time. This will provide an insight into the implementation of the ternary system in sensing applications.

2. Experimental details

2.1 Synthesis method

The synthesis was performed in two phases; initially, the metal complex with polyacrylamide was prepared *via* frontal polymerization and then a sensing film of $Cu_{0.8}Zn_{0.2}Sb_2$AAm was fabricated using a spin coating technique.

2.2 Preparation of $Cu_{0.8}Zn_{0.2}Sb_2$AAm *via* frontal polymerization

The preparation of the monomer of $Cu_{0.8}Zn_{0.2}Sb_2$ nitrate AAm complex was carried out by a modified procedure (Fig. 1). Initially, the transition metal nitrates embedded in AAm complexes were prepared. For this $Cu(NO_3)_2{\cdot}3H_2O$ (0.77 g, 2.26×10^{-3} mol), $Zn(NO_3)_2{\cdot}6H_2O$ (0.136 g, 0.56×10^{-3} mol), $Sb(NO_3)_3$ (1.74 g, 5.66×10^{-3} mol) and AAm (2.0 g, 4.23×10^{-3} mol) were

Table 1 A detailed literature survey of other humidity sensing materials with % RH values

S. no.	Material	Sensitivity (pF/% RH)	Range (% RH)	Ref.
1	SnO_2 nanostructures	0.01	11–96	32
2	Fe–GO	5.18	10–95	33
3	Au/PVA	11.38	11.3–97	34
4	Polyimide	24.5	16–90	35
5	Graphene oxide	46.253	15–95	31
6	Modified MWCNT (dispersed in NMP)	6.41	10–90	39
7	Tin dioxide/reduced graphene oxide (RGO)	146.53	25–95	37
8	MoS_2-modified SnO_2	156.97	11–95	38
9	$Cu_{0.8}Zn_{0.2}Sb_2$AAm nanocomposite	168.477	10–95	Present paper

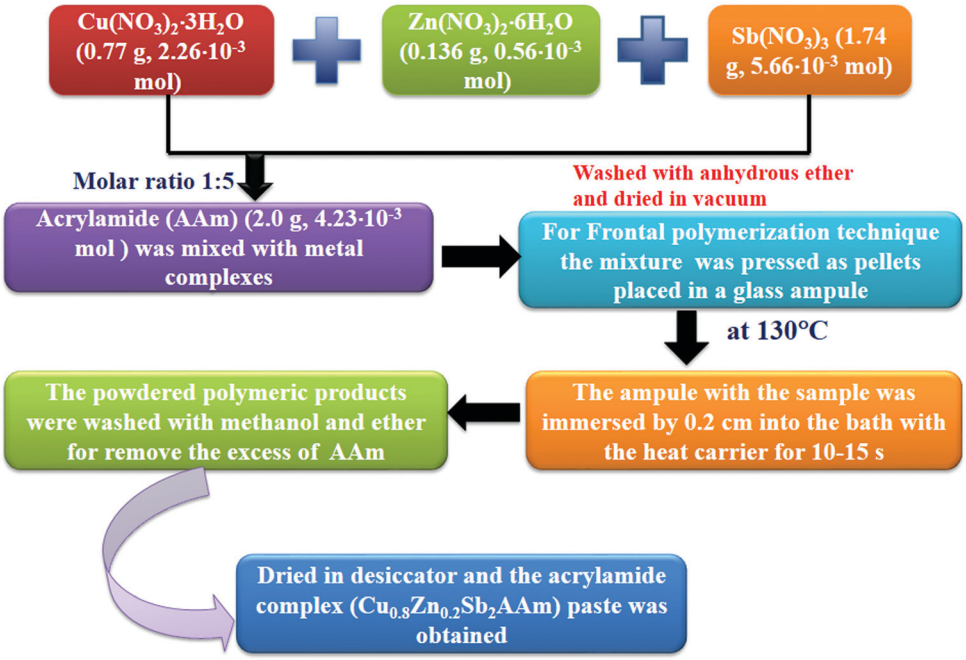

Fig. 1 Flow chart showing the synthesis of the polymer nanocomposite ($Cu_{0.8}Zn_{0.2}Sb_2AAm$).

mixed uniformly to maintain a metal : acrylamide polymer mole ratio of 1 : 5 in an inert atmosphere. After washing the homogenous mixture, a green paste was obtained and then dried in a desiccator for one day over P_2O_5. Next, the paste was rewashed with methanol and ether to remove the excess AAm. The paste was dried again in a desiccator for 24 h to a constant weight and the fine paste of $Cu_{0.8}Zn_{0.2}Sb_2AAm$ was obtained. After the preparation of the monomer, the $Cu_{0.8}Zn_{0.2}Sb_2AAm$ sample was used for the frontal polymerization technique, where the acrylamide complex was pressed into a pellet with fixed dimensions; the diameter d of the pellet was 0.5–0.8 cm, the height h was 1.2–1.5 cm, and the density ρ was 1.45 $\pm$ 0.02 g cm^{-3}. Next, this pellet was placed in a glass test tube, and to initiate the polymerization, the bottom region of the test tube containing the sample was immersed 0.2 cm into a bath with Wood's metal alloy as the heat carrier for 10–15 s at 130 °C. The reaction rate was monitored from the movement of the front of the colored zone over time. Next, the powder was washed several times with methanol and ether to remove excess AAm and then dried in a vacuum at room temperature for 24 h. Thus, $Cu_{0.8}Zn_{0.2}Sb_2AAm$ powder was obtained and used for further characterization and then in a humidity sensor application.

2.3 Experimental set-up for the photoconduction measurements

The room temperature photoconduction properties of the prepared samples were recorded using a 6517B source measuring unit (SMU, Keithley, UK) in the resistance mode at an illumination intensity of ~100 mW cm^{-2}. Fig. 2 shows the schematic diagram of photoconductive device based on the $Cu_{0.8}Zn_{0.2}Sb_2AAm$ nanomaterial.

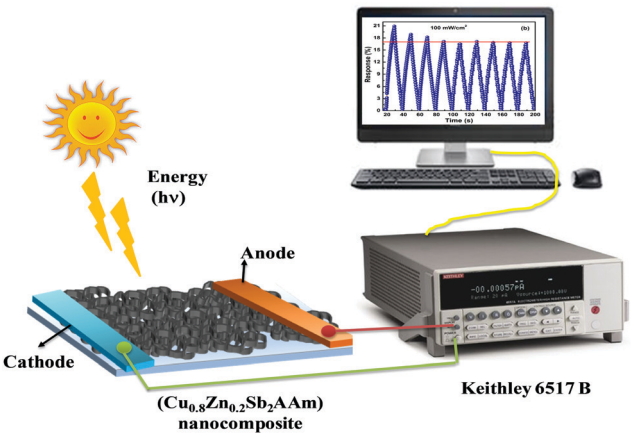

Fig. 2 A schematic diagram of the photoconduction set-up.

2.4 Fabrication of the thin film

A thin film based sensing element was fabricated by a spin coating technique which is shown in Fig. 3.

The uniformity in the deposition of the film was influenced by key parameters such as rotation of the spinner, and temperature and viscosity of the solution. Initially, borosilicate substrates having uniform dimensions of 1.5 × 1.5 cm^2 were treated in an ultrasonic cleaner (WUC-AO2H, Witeg, Germany) using de-ionized water, isopropyl alcohol and acetone as a cleaning agent. The solution was coated on the glass substrate using a spin coater (RC100, Metrex India) with an angular rotation of 2000 rpm and further dried for 30 min at 60 °C. The fabricated film was then annealed at 200 °C for 2 h in a tubular electric furnace for the complete removal of organic components. Probe contacts were developed on both the ends

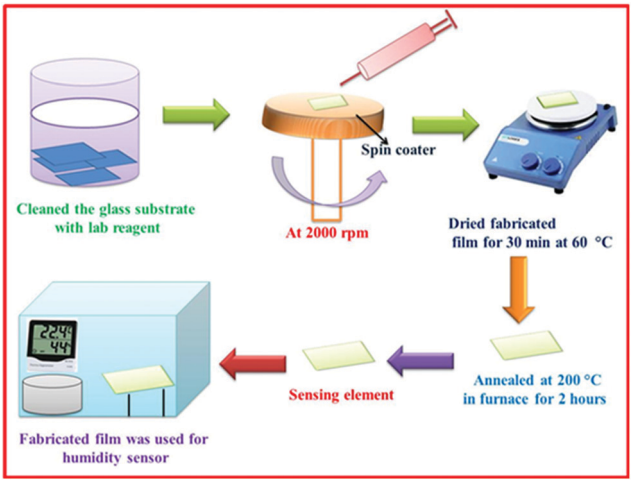

Fig. 3 A schematic presentation of the preparation of $Cu_{0.8}Zn_{0.2}Sb_2AAm$ film *via* a spin-coating method.

of the thin film using a silver paste with a copper wire connecting with them, which acted as electrodes. Thus, this film was employed as a sensing element for the detection and measurement of humidity.

3. Results and discussion

3.1 Morphological investigation (SEM analysis)

A porous surface morphology of a thin film is a key feature for a humidity sensing application. Surface morphology of the as-fabricated $Cu_{0.8}Zn_{0.2}Sb_2AAm$ thin film was investigated using SEM (JSEM-6490LV, Jeol) at different magnifications and the images are shown in Fig. 4(a–d). It was confirmed from the images that the surface morphology of the $Cu_{0.8}Zn_{0.2}Sb_2AAm$ thin-film possessed a highly porous structure with intermediate voids on the surface being responsible for the characteristic adsorption and desorption of humidity. The high surface to

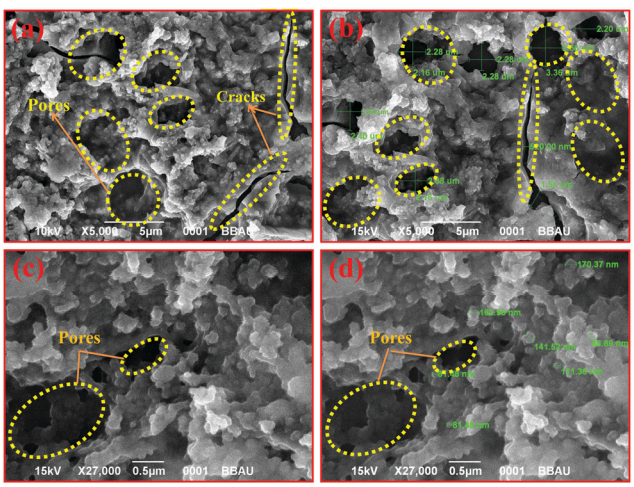

Fig. 4 SEM images (at different scales) showing that the morphology of the $Cu_{0.8}Zn_{0.2}Sb_2AAm$ thin film possesses a highly porous rigid structure with few cracks and pores on the surface.

volume ratio confirmed its applicability for humidity sensing because a higher ratio facilitates the increase in active sites of the material which regulates the desorption/adsorption of humidity.[13,40,41] Consequently, the mesoporous nature of the $Cu_{0.8}Zn_{0.2}Sb_2AAm$ thin film exhibited a higher surface area solely responsible for the high sensitivity of the sensor at an ambient temperature. The presence of active sites on the surface comprised of dangling bonds encouraged high sensitivity over a short period. This favors the strong adhesion of water vapors that come in to contact with the surface.[12,42]

3.2 Brunauer–Emmett–Teller (BET) analysis

The porosity and surface area are the critical parameters that affect the sensitivity of a material. So the responsible surface area of the $Cu_{0.8}Zn_{0.2}Sb_2AAm$ thin film and the corresponding pore size distribution were estimated by the BET method, from the nitrogen (N_2) adsorption/desorption isotherms at 77 K (Autosorb-1, Quantachrome, USA). For the $Cu_{0.8}Zn_{0.2}Sb_2AAm$ thin film, the specific surface area was found to be 2.0 $S_{ep}/m^2\ g^{-1}$, whereas the pore volume and pore radius were estimated to be 0.0084 V $cm^{-3}\ g^{-1}$ and 82.4 Å, respectively, see Fig. 5(a and b).

3.3 XRD analysis

The influence of incorporating metal ions in the polymer matrix was reflected in the crystalline nature of the host polymer.[43,44] This influence was investigated using the XRD diffraction pattern of the $Cu_{0.8}Zn_{0.2}Sb_2AAm$ thin film shown in Fig. 6. It can be easily seen from the diffraction pattern that the crystallinity of the host PAam decreases with the addition of Cu, Zn and Sb metal ions.[45,46] Here, the high-intensity peaks corresponding to Cu, Zn, and Sb were also observed at 2θ values of 24.01°, 28.94°, 40.42°, and 51.25°. Thus, the diffraction pattern obtained confirmed the polycrystalline nature of the $Cu_{0.8}Zn_{0.2}Sb_2AAm$ thin film. The minimum crystallite was calculated to be 19 nm using the Debye Scherrer formula.

3.4 Transmission electron microscopy (TEM) analysis

Fig. 7 shows the TEM image of the $Cu_{0.8}Zn_{0.2}Sb_2AAm$ thin film at a 20 nm scale with an inset SAED image showing the circular fringes. These circular fringes reveal the periodic distribution among the crystal giving a well-defined diffraction pattern. The TEM image confirms the well-defined crystalline nature of the metallopolymer with oval-shaped voids on the surface of the $Cu_{0.8}Zn_{0.2}Sb_2AAm$.

3.5 Particle size analysis

The particle size of an aqueous solution of poly-CuZnSbAAm complex was determined using a particle size analyzer (Zetasizer Nano-ZS90, Malvern Panalytical) and the resultant data is plotted in Fig. 8(a). The particle size analysis obtained from the dynamic scattering of light phenomena. From Fig. 8(a) the particle size distribution curve shows that the peaks are divided into two major intensities, the first one is the peak of the particles at ~21 nm with the neighboring peak at 50 nm.

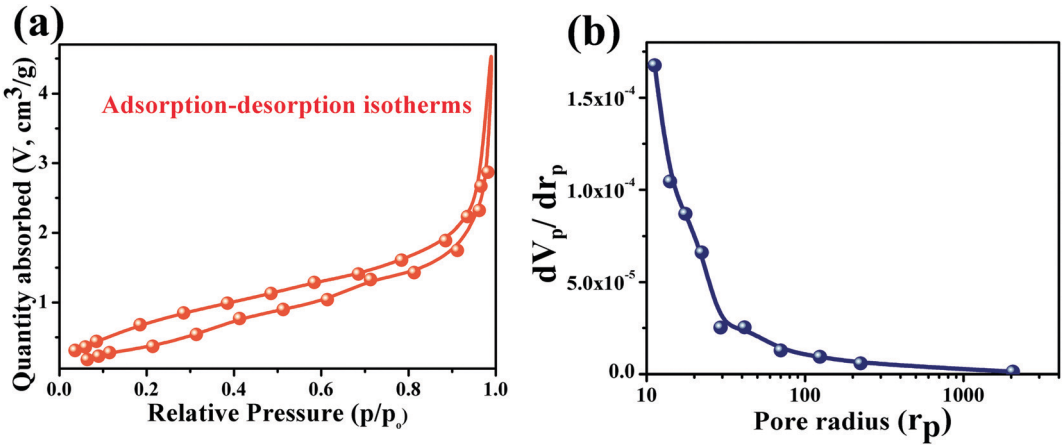

Fig. 5 (a) Adsorption–desorption isotherms of $Cu_{0.8}Zn_{0.2}Sb_2AAm$, and (b) pore radius distribution curves relative to variations in pore volume.

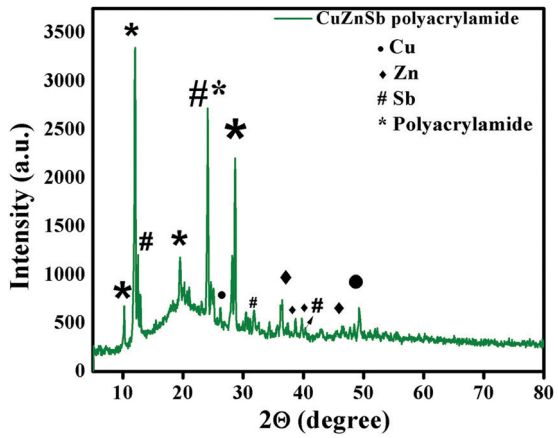

Fig. 6 The XRD pattern of $Cu_{0.8}Zn_{0.2}Sb_2AAm$, which confirms the crystalline nature and the presence of Cu, Zn and Sb *via* their characteristic peaks.

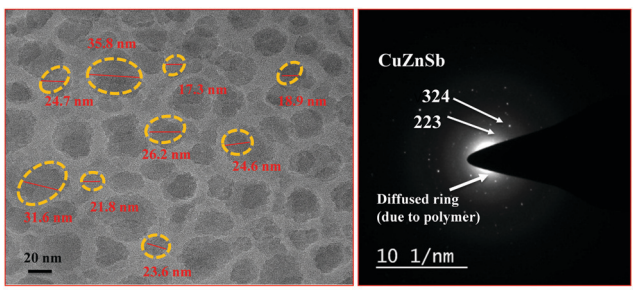

Fig. 7 (a) A TEM image of the $Cu_{0.8}Zn_{0.2}Sb_2AAm$ thin film, and (b) the SAED pattern of $Cu_{0.8}Zn_{0.2}Sb_2AAm$.

3.6 UV-visible absorption analysis

The UV-visible absorption analysis was carried out using a spectrophotometer (Evolution 201, ThermoScientific). The absorption spectrum was recorded in the wavelength range from 190 to 1100 nm. Singh and co-workers, reported that the principal band of pure acrylamide appears at 197 nm,[47,48] whereas in this case the characteristic band of the CuZnSb Aam complex has been found at 320 nm due to the complexation between the metal ion and the PAam polymer. In Fig. 8(b), the variation of absorbance with the wavelength is shown with an *in situ* plot between the optical absorption coefficient (α) and photon energy ($h\nu$) known as the Tauc plot. The optical band-gap E_g of the $Cu_{0.8}Zn_{0.2}Sb_2AAm$ thin film was calculated using the formula:

$$\alpha h\nu = A(h\nu - E_g)^n$$

where ν is defined as the transition frequency, A is a constant and n is the value of allowed transitions characteristic to the nature of the material. The direct band transitions, n = 1/2 and 3/2 correspond to allowed and forbidden transitions, respectively, while for indirect transitions, n = 2 and 3 relate to allowed and forbidden transitions, respectively. For this material, the transition is the direct allowed type, therefore, n = 1/2 was used in the previous formula for the calculation of the optical bandgap. The optical band gap E_g was estimated by extrapolating the straight line where α = 0 on the $(\alpha h\nu)^2$ *vs.* $h\nu$ (Tauc plot) curve and it was found to be 3.91 eV.

3.7 IR spectroscopy studies

The IR spectroscopic analysis is shown in Fig. 9. Several peaks in the IR spectra indicate that the metal atom is coordinated to the oxygen atoms of the carbonyl group of the AAm ligand. The partial shift of ν(CO) vibration bands (1676 cm^{-1}) towards the longer wavelength region, is in agreement with the results of previous transition metal complex analysis. The spectra of the complexes contain the footprints of the vibration bands of the nitrate anion at 1384 cm^{-1} ($\nu(NO_3)$) together with the stretching and deformation vibration bands of the NH-groups (ν_s NH and ν_{as} NH at 3184 cm^{-1} and 3352 cm^{-1}, respectively, and δNH at 1612 cm^{-1}). The vibrations of the vinyl bond: 812 cm^{-1}, 980 cm^{-1} *d* (out-of-plane deformation mode of $=CH_2$), 1052 cm^{-1} (stretching mode of =CH–C), were observed in the range of 810–1000 cm^{-1}. Due to an overlap of the strong νCO absorption band with the >C=C< band, the latter was not observed in the complex.

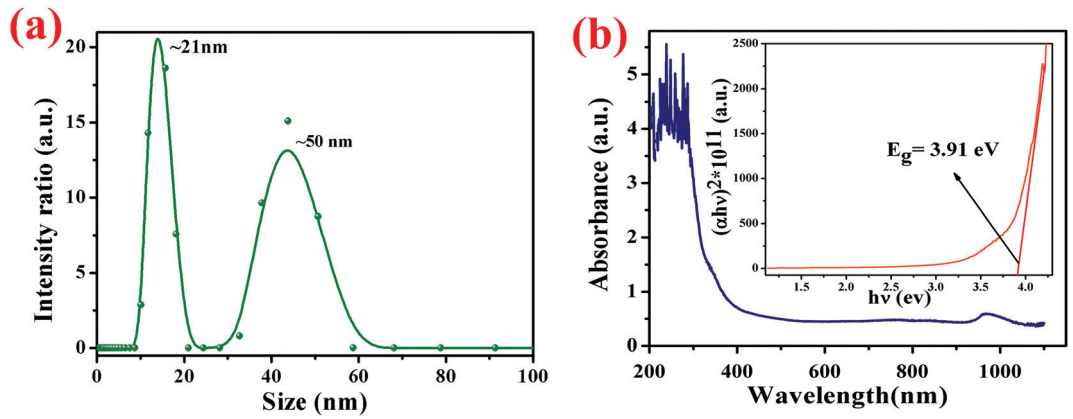

Fig. 8 (a) The particle size distribution curve shows that the peaks are divided into two major intensities; the first one is the peak of the particles at ~21 nm with a second neighboring peak at 50 nm. (b) The optical absorbance spectrum of the fabricated film in the wavelength range of 190–1100 nm; the inset shows the Tauc plot.

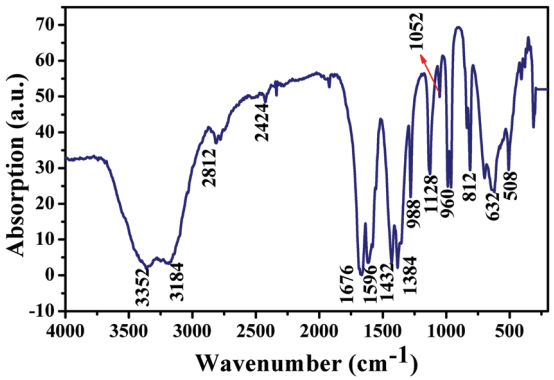

Fig. 9 The IR spectrum of the $Cu_{0.8}Zn_{0.2}Sb_2$AAm thin film.

3.8 Thermogravimetric analysis

Fig. 10 reveals the thermogravimetric degradation results of the $Cu_{0.8}Zn_{0.2}Sb_2$AAm, measured from 35 °C to 400 °C in a N_2 atmosphere. From the figure, successive decomposition can be observed with an increase in temperature. There are mainly two regions as observed in the curve. Initial weight loss was observed at 35–200 °C due to the absorption of heat and later on successive evaporation of water vapour was seen above 100 °C. In this region, the weight loss was observed to be 44.44% of the initial weight. The second major weight loss was observed during the temperature range of 200–400 °C due to thermal decomposition of the gases and removal of functional groups such as CO, OH and NH_2 of the polymer, with a degradation of about 33% and the final thermal decomposition of $Cu_{0.8}Zn_{0.2}Sb_2$AAm occurred beyond 400 °C, caused by the thermal deformation of the polymer.[46] This analysis showed that CuZnSb AAm was more stable than the AAm with an increased decomposition temperature of 400 °C.

3.9 Differential scanning calorimetry (DSC)

Calorimetry is particularly useful in the study of crystallization as it provides a direct measurement of thermodynamic properties, for example, heats of fusion, melting temperatures, and so on. Insertion of metal ions within the polymer matrix drastically influences the thermal characteristics of the parent polymer. To investigate the thermal behaviour of $Cu_{0.8}Zn_{0.2}Sb_2$AAm, the bonded metal ions embedded in polymer matrices which produce a higher number of charge carrier ions causing rigidity enhancement in the polymer chain up to the optimum metal salt

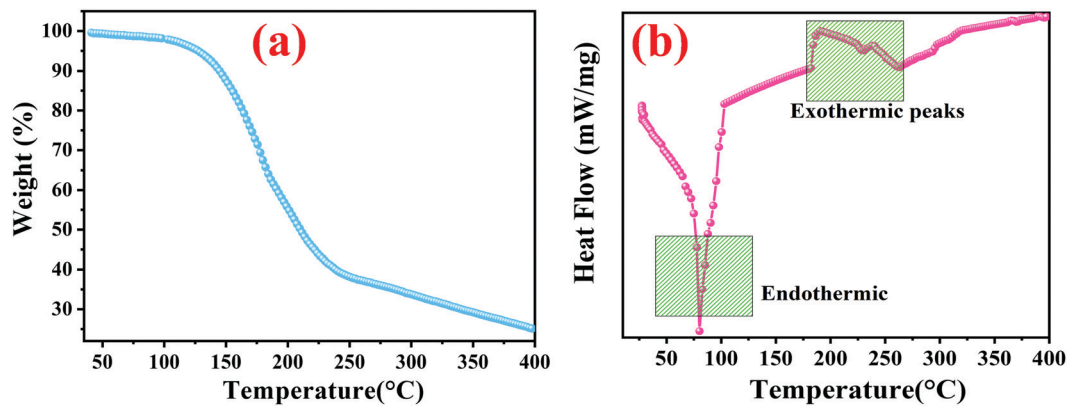

Fig. 10 (a) TGA and (b) DSC curves of $Cu_{0.8}Zn_{0.2}Sb_2$ AAam under an argon atmosphere at a heating rate of 10 °C per minute.

concentration were investigated. Consequently, the T_g reached a higher value as shown in Fig. 10(a). The DSC analysis was performed in a temperature range from 35–400 °C in the presence of N_2. The DSC curve for $Cu_{0.8}Zn_{0.2}Sb_2$AAm is shown in Fig. 10(b). It is worth noting from the curve the presence of one sharp endothermic peak with two wider exothermic peaks were confirmed at temperatures of 81.5 °C, 195 °C and 238.7 °C, respectively.

4. X-ray photoelectron spectroscopy (XPS) analysis

The chemical composition of the $Cu_{0.8}Zn_{0.2}Sb_2$ AAam nanocomposite was confirmed by XPS analysis and the results are shown in Fig. 11(a–f). The XPS results show the binding energies of the Cu, Zn, Sb, C, N and O elements with their corresponding atomic weight%. Characteristic peaks of Cu are shown in Fig. 11(b) having the binding energies of 933 eV and 953.3 eV, which corresponded to two states, Cu $2p_{3/2}$ and Cu $2p_{3/2}$, respectively.[48] The presence of zinc (Zn 2p) is also confirmed from Fig. 11(c) which shows the binding energies of 1022.7 eV and 1045 eV corresponding to the energy states of Zn $2p_{3/2}$ and Zn $2p_{1/2}$, respectively.[47] The presence of antimony was also observed from Fig. 11(d), where the electronic states of this element are Sb_2O_3 and $Sb_3d_{3/2}$, which matches well with the binding energies of 532.14 eV and 540 eV.[49] The remaining elements, O, C and N have two broad peaks of carbon as shown in Fig. 11(e). The binding energies of 285 eV and 288 eV confirmed the presence of the (C–C, C–O) and O–C=O, respectively. Fig. 11(f and g) shows the presence of O and N elements with binding energies of 532 eV and 400 eV which confirmed the presence of the energy states of O 1s(C–O) and N 1s.[49] The histogram plot of atomic weight % and the binding energies can be seen in Fig. 11(g and h).

5. Photoconduction analysis

The photoconduction behaviour of $Cu_{0.8}Zn_{0.2}Sb_2$ AAam nanocomposite was investigated under the exposure of white light to determine its applicability in energy-saving elements,

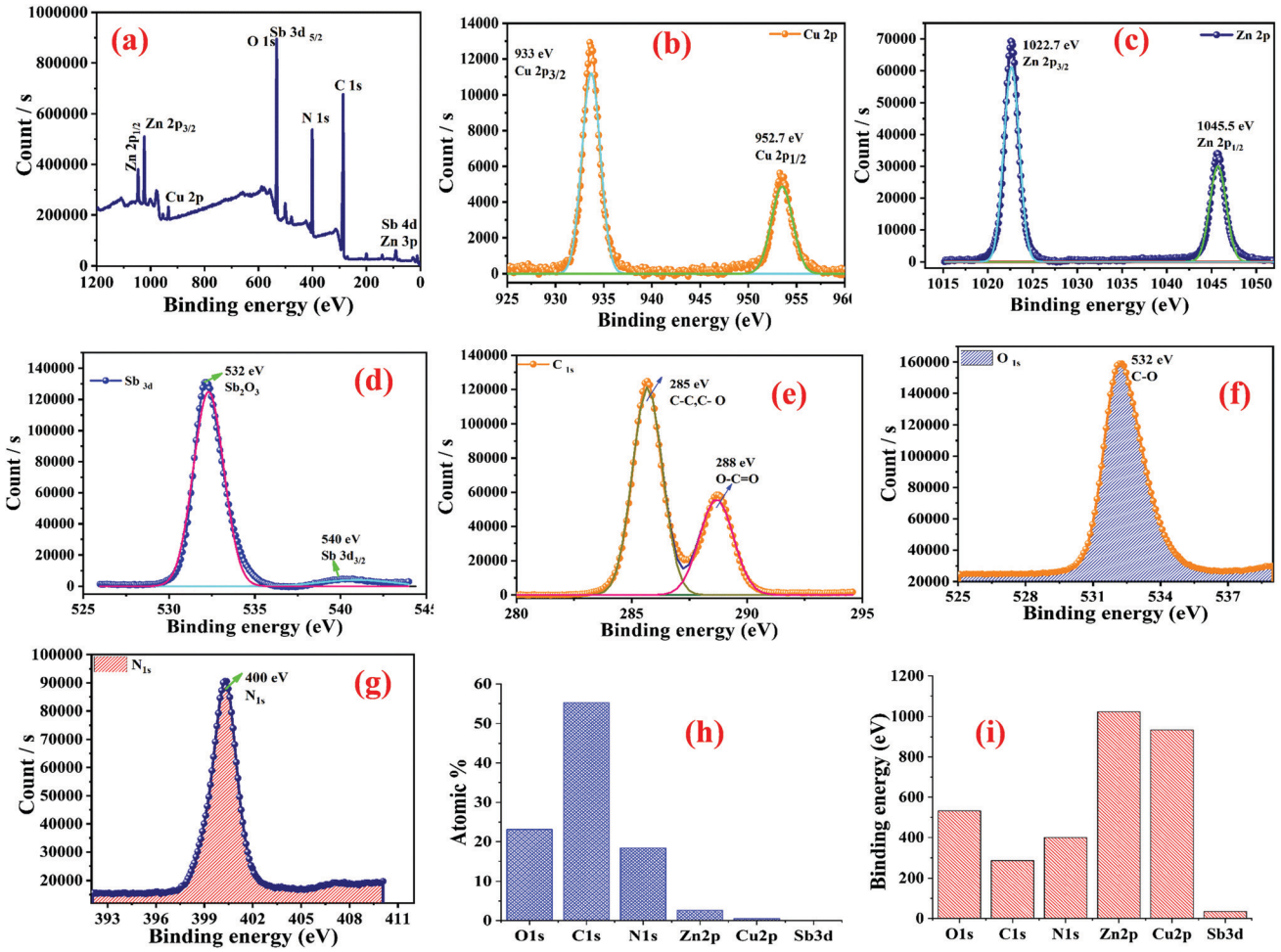

Fig. 11 XPS analysis of the $Cu_{0.8}Zn_{0.2}Sb_2$ AAam nanocomposite: (a) survey; (b) copper (Cu 2p) element; (c) zinc (Zn 2p) element; (d) antimony (Sb 3d) element; (e) carbon (C 1s) element; (f) oxygen (O 1s) element; (g) nitrogen (N 1s) element; (h) atomic weight% values of the elements; and (i) a histogram showing the binding energies of the nanocomposites.

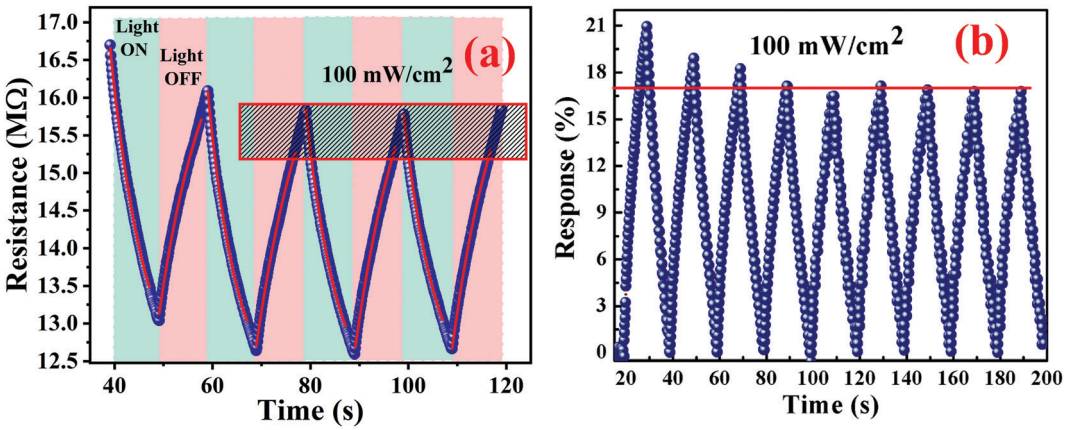

Fig. 12 (a and b) Photoconduction behaviour of the $Cu_{0.8}Zn_{0.2}Sb_2AAm$ nanomaterial.

light-dependent resistors, and so on, and the characteristic curve is shown in Fig. 12(a and b). Fig. 12(a) shows the variation of change in electrical resistance with respect to time at 100 mW cm^{-2} power intensity and Fig. 12(a) shows the photodegradation and saturation in the polymer nanocomposite after a few cycles of response and recovery. This maximum response accompanied by a saturated response may be due to the polymeric nature of the metallopolymer nanomaterial. Successive changes in the electrical resistance of the thin film under the illumination of white light was measured. On exposure of light, the reduction in resistance showed a generation of excess carriers in the $Cu_{0.8}Zn_{0.2}Sb_2AAm$ nanomaterial.

The resistance measurement was executed in two conditions: initially in the dark and then in the light at ambient temperature under the exposure of a light beam having a power intensity of ~100 mW cm^{-2}. Hence, it was found that the nanomaterial performed as a photoconductive material. The photoresponse was evaluated by using the following equation:

$$\%\ \text{Respose} = \frac{R_d - R_l}{R_d} \times 100 \quad (1)$$

where R_d and R_l are the electrical resistance in dark conditions and light conditions, respectively. The excess carriers in the photoconductive nanomaterials were generated simultaneously; they start by recombining with nearby counterparts. This change in electrical resistance of the sample can be accounted for by the conduction of unrecombined photoexcited charge carriers. For a better understanding of the conduction of charge carriers, the following equation can be used:

$$\Delta R = \frac{l}{q\mu dt\Delta n} \quad (2)$$

where l, d, and t are the length, width and thickness of the sample, respectively, q and μ are the electronic charge and mobility, respectively, and Δn is the change in charge carrier concentration in the presence of light.

When the light beam is incident on the surface of a material, photons of the ray interacted with the material causing the generation of electron–hole pairs. The generated electron–hole pairs at a different junction in the sample can easily be separated from each other. Due to sufficient excitation energy, the electrons transition from the valence band to the conduction band. After the first few cycles of change in resistance, the photoresponse of the nanomaterial gets stabilized at ~17.1%. This may also be possible because of the combined effect of slight photodegradation and an increase in the concentration of electron–hole pairs. The representative curve shows a sawtooth wave characteristic which implies that the response changed subsequently with time and was repeatable. In the light region, the material follows a dramatic drop in resistance value. However, when the light is turned off, the material almost regains its original state which is also a requirement of a photoconductive nanomaterial. The highly sensitive polymer nanocomposite $Cu_{0.8}Zn_{0.2}Sb_2AAm$ has a narrow optical band gap which provides the larger surface area, and because of this reason the active sites of the material are responsible for the electron–hole pair generation through the photon–phonon interaction. This phenomenon leads to the enhanced photoconductive properties of the material. The resistance of material in the presence of light and dark regions can be given by the following equations:

$$R_l = R_0 \exp\frac{-t}{\tau_{res}} \quad (3)$$

$$R_d = R_0\left\{1 - \exp\left(\frac{-t}{\tau_{rec}}\right)\right\} \quad (4)$$

where R_0 is the electrical resistance in the dark region, and τ_{res} and τ_{rec} are the response and recovery time, respectively. The response time is defined as the time taken to obtain 90% of the maximum resistance. The response and recovery times are very important properties of any photoconductive device, therefore, the response and recovery time of $Cu_{0.8}Zn_{0.2}Sb_2AAm$ nanomaterial was evaluated and found to be 6.6 s and 10.24 s, respectively. The response and recovery times have been evaluated in this work and were found to be quite good and highly comparable with other reported results. These data are shown in Table 2.

Table 2 A comparative study of response and recovery times from the literature

Material name	Synthesis method	Response time (s)	Recovery time (s)	Ref.
MoS_2	Chemical vapour deposition	20	10.97	50
SnSe	Chemical vapour deposition	8.2	5.3	51
WS_2	Chemical vapor deposition	51	88	52
Phosphorus	Electrochemical exfoliation	15	30	53
V_2O_5	Hydrothermal method	65	75	54
$Cu_{0.8}Zn_{0.2}Sb_2$AAm nanomaterial	Frontal polymerization	6.6	10.24	This work

6. Humidity sensing measurements

The hydrophilic nature of the $Cu_{0.8}Zn_{0.2}Sb_2$ AAm favors its humidity sensing properties. Morphological features of the as-synthesized thin-film strongly encourage the adsorption/desorption on the surface. The presence of mesoporous voids provides more chemical affinity towards water molecules.[14,55] These physical and chemical properties of $Cu_{0.8}Zn_{0.2}Sb_2$ AAm, in turn, improve the sensitivity of the film.

To examine the deterministic features of the $Cu_{0.8}Zn_{0.2}Sb_2$ AAm thin-film sensor, the sensing characteristics were tested under the frequency range of 20 Hz to 2 MHz at ambient temperature. Later on, the humidity-sensing performance of $Cu_{0.8}Zn_{0.2}Sb_2$ AAm thin-film sensor was investigated under various levels of humidity (% RH) shown in Fig. 13(a and b). Because the sensitivity curve, response time and recovery time, and stability are the key parameters which authenticate the reliability of this material as a humidity sensor these parameters were plotted and are discussed in this paper.

It has been observed that as the value of the operating frequencies increases, there is a gradual decrease in the capacitance of the film.[56,57] The maximum capacitance value at 95% RH was found to be 10 000 pF at a frequency of 20 Hz whereas the lowest capacitance value was found at 20 MHz. The same trend was observed for both adsorption and desorption processes. It has been observed that as humidity (% RH) increases from 33% to 95%, the value of capacitance increases monotonically following the same trend. Because the relative humidity level increases, the output capacitance of the sensor ultimately reached a higher value. The cause responsible for this behaviour is the adsorbed water molecules which empower the polarization process and due to this polarization, the dielectric constant of the

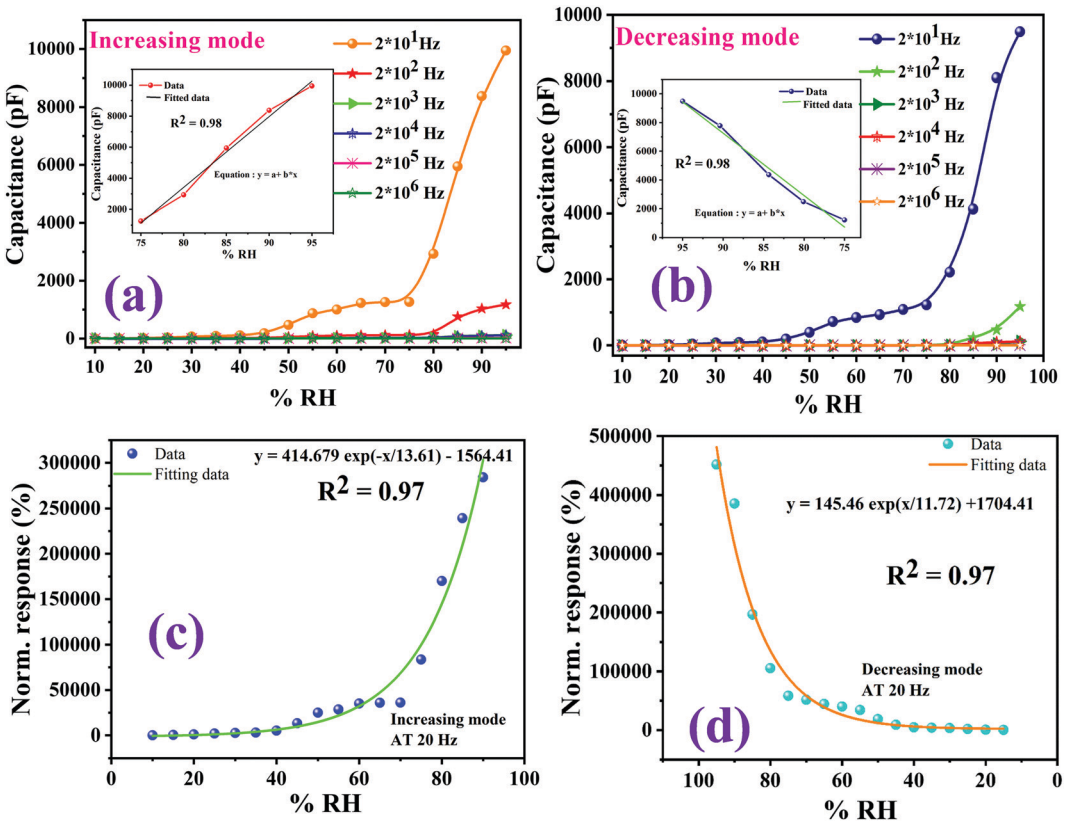

Fig. 13 Humidity sensor response curves at room temperature. (a) The variation of capacitance corresponding to the variation of % RH in an increasing mode at different frequencies (20 Hz to 2 MHz). (b) The capacitive humidity sensor curves at different frequencies in a decreasing mode. (c and d) The normalized responses *via* an exponential data fitting function for increasing mode and decreasing mode.

sensing element increases. This, in turn, affects the capacitance.[58,59] Among the various test frequencies, 20 Hz exhibits the best linearity for humidity sensing characteristics, so this frequency was selected for determining the other sensing characteristics. The $Cu_{0.8}Zn_{0.2}Sb_2$AAm polymer nanocomposite sensing film showed a linear curve from the 70–95% RH in an increasing mode and 95–75% RH in a decreasing mode at a 20 Hz frequency, which are shown as an inset in Fig. 13(a and b). In Fig. 13(c and d), the normalized sensor response with the exponential data fitting curves as a function of %RH for nanocomposite at 20 Hz frequency is also provided.

The dependency of capacitance and frequency under the influence of different % RH values were thoroughly investigated and the results are shown in Fig. 15(a). The variation of capacitance with operating frequency exhibited an excellent characteristic trend.[58–60] It is obvious from the curve that the capacitance (C) changed with increases in frequency. Interestingly, the level of decrease in capacitance value was faster at higher % RH levels compared to lower % RH values. The capacitance value increased with % RH in the lower frequency range (below 2 kHz) and in the higher frequency range, the change in capacitance was almost negligible and became independent of the humidity conditions.[61] Humidity seems to be ineffective at a frequency beyond 2 kHz. The ideal capacitive sensor inherited this property, *i.e.*, the value of capacitance was independent of applied frequency. In low humidity conditions, the sensing material absorbed a small quantity of water, thus acting as a favourable circumstance for an ideal capacitive sensor.[61,62] This is because the electric field direction changed gradually at low frequencies with the appearance of space-charge polarization in adsorbed water when the frequency was high, the electrical field direction changes so fast that the polarization of the adsorbed water cannot be connected with it, and hence, the dielectric constant was small and independent of relative humidity.

From Fig. 14(b), it can be observed that the value of capacitance was influenced by the frequency (20 Hz–2 MHz). The relative humidity (10–95% RH) affected the sensitivity of the material which varied with the frequency variation. It can easily be seen that at a frequency of 20 Hz, the capacitance increased rapidly with the relative humidity and the value of capacitance changed from 3.5 pF to 9486 pF which gave the average sensitivity of $S \sim 168.477\%$. However, at a frequency of 2 MHz, a small change in capacitance, from 3.6 pF to 4.59 pF, was found which corresponded to the sensitivity of $S \sim 0.004\%$ across the RH range of 10–95%. Thus, the major difference in the sensitivity was observed at 20 Hz, and this value was chosen as the optimum frequency for this sensor and is shown in Fig. 14(b). The sensitivity of the humidity-dependent capacitive $Cu_{0.8}Zn_{0.2}Sb_2$ AAm thin-film is defined as:[57]

$$\text{Sensitivity} = \frac{C_{\text{final}} - C_{\text{initial}}}{\text{RH}_{\text{final}} - \text{RH}_{\text{initial}}} \quad (5)$$

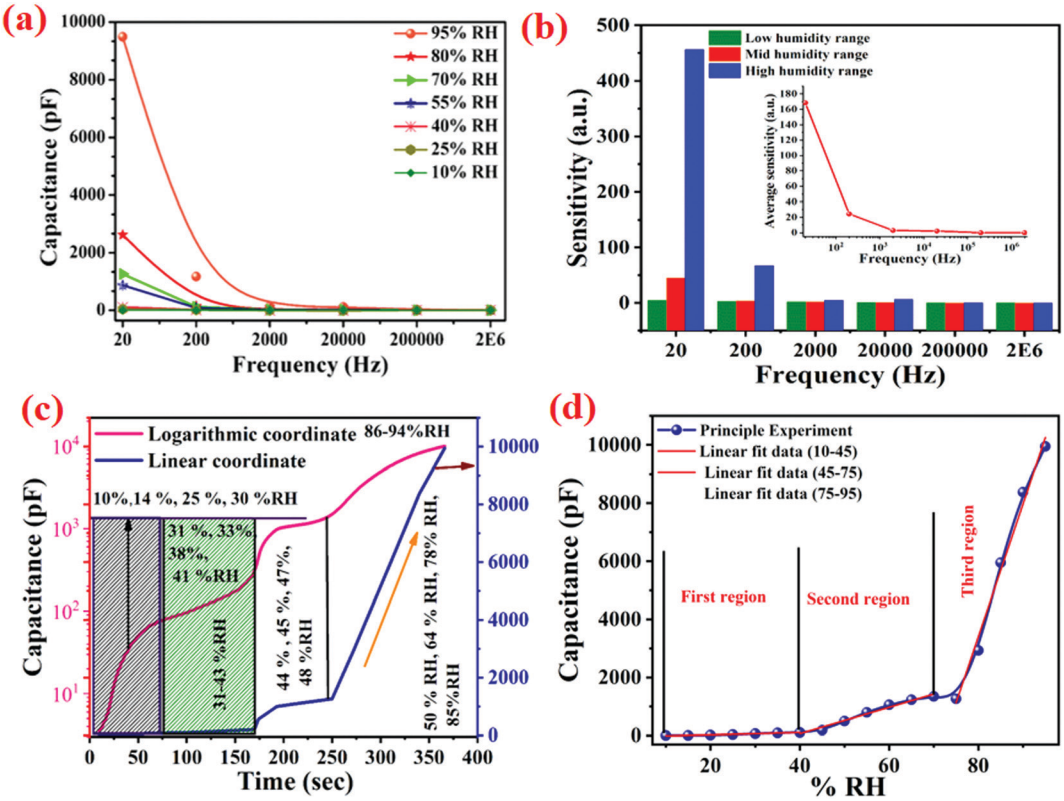

Fig. 14 (a) Variations of capacitance with frequency at different % RH values (10–95% RH) for a Cu–Zn–Sb PAam thin-film based humidity sensor at room temperature. (b) The sensitivity response at different test frequencies at 25 °C to different % RH values. (c) The humidity sensor response on the logarithmic scale, and (d) a linear fitted curve for sensitivity calculations.

Table 3 Sensitivity of the $Cu_{0.8}Zn_{0.2}Sb_2AAm$ polymer nanocomposite at different frequencies

Frequency	Low-humidity region (10–45% RH)	Mid-humidity region (45–75% RH)	High-humidity region (75–95% RH)	Average sensitivity (pF/% RH)
2×10^1 Hz	3.890	45.466	456.076	168.477
2×10^2 Hz	2.801	3.562	66.980	24.447
2×10^3 Hz	1.890	2.145	4.961	2.998
2×10^4 Hz	0.161	0.552	5.990	2.234
2×10^5 Hz	0.002	0.006	0.041	0.016
2×10^6 Hz	0.001	0.004	0.009	0.004

where C_{final} and $C_{initial}$ are the capacitive values at the final and initial % RH levels, respectively. Fig. 14(b) shows that the frequency affects the sensitivity of the material. Fig. 14(c) shows the humidity sensor response curve of capacitance and time. The linear coordinate curve is shown as a blue line whereas the logarithmic coordinates are shown as a pink line. There is a non-linear curve over the whole range (10–95% RH). Fig. 14(d) displays the sensitivity calculation for the linear data fitting of the adsorption curve at 20 Hz, and as is known the sensor response curve shows the exponential change between capacitance and humidity.[21,63] The humidity is linearly fitted into three regions 10–45% RH, 45–75% RH and 75–95% RH, and the values of the slope obtained are shown in Table 3.

6.1 Stability

Stability is a very important parameter for any sensor. The reliability of any sensor for long term operation corresponds to its stability over a certain duration of time. The stability characteristics of sensing elements operating at a frequency of 20 Hz under different % RH values, *e.g.*, 15%, 35%, 55%, 75%, and 95% for 60 d, were monitored. The measurements of the humidity sensing parameters were repeated every five days (Fig. 15). The stability curve shows a 4% variation in the capacitance at this operating frequency. This shows that the consistency of the sensing capability of PAam film makes it suitable for the purpose for which it was fabricated.

6.2 Response and recovery

Response and recovery times are the essential demands which significantly define the performance of a humidity sensor.

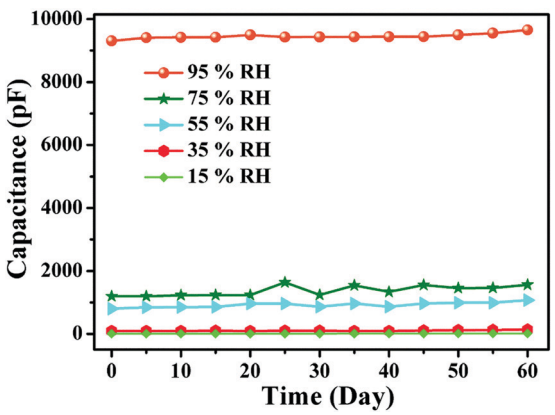

Fig. 15 Stability curve of the sensing element at different % RH values.

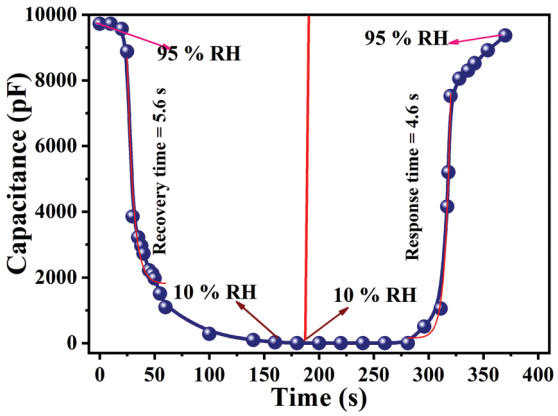

Fig. 16 A response curve showing a response time of 4.6 s and a recovery curve showing a recovery time of 5.6 s.

Sensors with short response and recovery times are the best for applications and commercialization. The time taken by a sensor to accomplish ~95% of the total capacitance change is defined as the response time in case of adsorption or termed as the recovery time in the case of desorption of water vapour.[10,56,64] Both response and recovery time are plotted in Fig. 16. Consequently, the sensor response time (humidity from 10% RH to 95% RH) and the recovery time (desiccation from 95% RH to 10% RH) were calculated to be 4.6 s and 5.6 s respectively. In comparison to the conventional polymer-based humidity sensors, the $Cu_{0.8}Zn_{0.2}Sb_2$ acrylamide thin-film sensor has proven to be better.[55–62,64] These exceptional characteristics occur because of the repeating units of the monomer $CH_2CH(CONH_2)$. The nitrogen forms hydrogen bonds with water molecules resulting in a strong hydrophilic nature and can form aqueous solutions of a very high concentration. Polymers are generally gel forms and due to their gel-like properties, these polymers are widely employed as flocculants in the removal of suspended particles from sewage and industrial effluents.

6.3 Sensing mechanism

The mechanism devoted to the electrical response of the sensing element upon exposure to humidity is the chemical and physical adsorption of water molecules on the surface of the sensing element. A particular concern with a capacitive-based humidity sensor is the relationship between the capacitance and the % RH can be expressed by the following equation:

$$C = \left(\varepsilon_r - i\frac{\gamma}{\omega\varepsilon_0}\right)C_0 \quad (6)$$

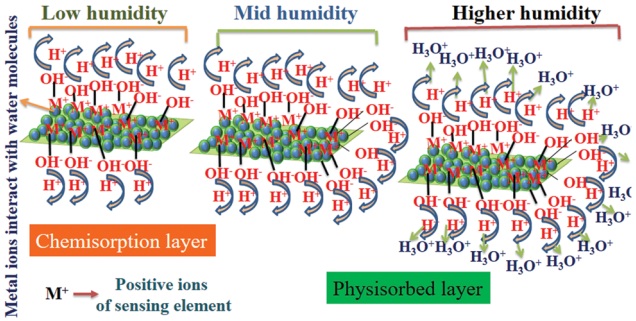

Fig. 17 A schematic presentation of the humidity sensing mechanism on the surface of the film; three regions are shown at low, medium, and high levels of % RH.

where C indicates the conductance and ν represents applied frequency. From eqn (6), it is clear that the capacitance of the sensing element is proportional to C_0, whereas C is inversely proportional to the operating frequency.[56,58–61,64] The C_0 is related to the physisorption of water molecules on the sensing film so that different adsorption processes yield different conduction values. From the formula, it is obvious that the capacitance increases with rising RH, and also depends on the frequency.

Fig. 17 shows the humidity sensing mechanism, and despite the minimal surface area of the thin film, the presence of metals provided more surface-active sites in the form of M^+ ions to bond with the OH^- causing the formation of the initial chemisorption on the sensor surface. Initially, at a lower % RH, water molecules were chemisorbed onto the available unsaturated nitrogen bonds (hydrophilic group) of the sensing film through double hydrogen bonding, and this was considered as the first-layer chemisorption of water. In this regime, it is hard for the water molecules to travel independently because of the strong attraction from the double hydrogen bonding. Successive proton hopping initiated between adjacent hydroxyl groups in the first chemisorbed layer of water influenced a greater amount of energy, thus exhibiting a strong electrical resistance. Later, a few protons are available on the surface of the polymer film which had been confined by irregular mobile layers. These protons still contribute to the leakage conduction, c, which ultimately increases the capacitance at low humidity. As the % RH increases, the multilayer physisorbed water molecules arise,[36,50] forming the physisorbed layer, with water molecules attached by single hydrogen bonding on the hydroxyl groups. Consequently, the water molecules become transportable, and were likely to appear as the bulk liquid. With the formation of a subsequent multilayer, physical adsorption and the decomposition of physisorbed water caused ionization under an electrostatic field to produce a large number of hydronium ions (H_3O^+) in the form of charge carriers. Thus, charge transport on the film took place *via* the conductivity of the material generated by a Grotthuss chain reaction. The charge transport expression is given as:

$$H_2O \rightarrow H^+ + OH^-$$

$$H_2O + H^+ \rightarrow H_3O^+$$

$$H_2O + H_3O^+ \leftrightarrow H_3O^+ + H_2O$$

Finally, at high % RH, the physisorbed water molecules will penetrate the interlayer of the sensing film. A large number of prevailing amide groups in the polymer facilitated proton migration. This leads to a sudden increase of the capacitance of the material, causing quite a high sensitivity at high % RH, which is very useful for the dielectric constant of the material.

7. Conclusions

A $Cu_{0.8}Zn_{0.2}Sb_2AAm$-based capacitive humidity sensor was successfully fabricated using a spin-coating technique and the photoconduction behaviour of the material was also investigated. The mesoporous morphology of the fabricated thin film energized the sensing capabilities of the film. The wide band-gap of 3.91 eV facilitates better conduction, accompanied by a synergistic interaction between the metal Cu–Zn–Sb ternary phase and PAAm, which boosts the sensitivity as well as the photoconductivity of the thin film based sensing element. The $Cu_{0.8}Zn_{0.2}Sb_2AAm$–polymer interfaces exhibited photoconduction behaviour, revealing response and recovery times of 6.6 s and 10.24 s, respectively. The humidity sensing characteristics of the film surface were evaluated based on the capacitive performance of the $Cu_{0.8}Zn_{0.2}Sb_2AAm$ based thin film humidity sensor. The average sensitivity (S) was found to be ~168.477 pF/% RH at an optimum frequency of 20 Hz. The thin-film-based sensor exhibited rapid response and recovery times of 4.6 s and 5.6 s, respectively, with 96% sensitivity retention after 60 d. Thus, this study of a $Cu_{0.8}Zn_{0.2}Sb_2AAm$ polymer-based capacitive humidity sensor provides insight into the use of a stabilized ternary system based on a polymer nanocomposite for humidity sensing and photoconduction applications.

Conflicts of interest

The authors declare that they have no conflicts of interest.

Acknowledgements

Priyanka Chaudhary is thankful for a BBAU UGC non-NET fellowship, and the authors gratefully acknowledge the Department of Science and Technology (DST), Government of India, for financial support in the form of the Indo-Russian project (Ref. no. INT/RUS/RFBR/P-148), and the Russian Foundation for Basic Research (Project No. 17-43-500631). Dr Ravi Kant Tripathi acknowledges the Government of India for providing research grant UGC sponsoring Dr D.S. Kothari's post-doctoral fellowship (No. F.4-2/2006(BSR)/PH/16-17/0054).

References

1 W. Sun, G. Zhang, L. Pan, H. Li and A. Shi, *Int. J. Polym. Sci.*, 2013, **2013**, 397027.
2 M. Friedman, *J. Agric. Food Chem.*, 2003, **51**, 4504–4526.
3 A. M. Schiller and T. J. Suen, *Ind. Eng. Chem.*, 1956, **48**, 2132–2137.
4 J. Xiang, C.-L. Ho and W.-Y. Wong, *Polym. Chem.*, 2015, **6**, 6905–6930.
5 R. Ramya, P. Sankar, S. Anbalagan and P. N. Sudha, *Int. J. Environ. Sci.*, 2011, **1**, 1323–1338.
6 D. K. Maurya, S. Sikarwar, P. Chaudhary, S. Angaiah and B. C. Yadav, *IEEE Sens. J.*, 2019, **19**, 2837–2846.
7 M. Kt and S. P, *Org. Chem.: Curr. Res.*, 2015, **4**(3), 1000143.
8 G. I. Dzhardimalieva, S. A. Semenov, E. I. Knerelman, G. I. Davydova and K. A. Kydralieva, *J. Inorg. Organomet. Polym. Mater.*, 2016, **26**, 1441–1451.
9 P. Chaudhary, S. Sikarwar, B. C. Yadav, G. I. Dzhardimalieva, N. D. Golubeva and I. E. Uflyand, *Sens. Actuators, A*, 2017, **263**, 415–422.
10 X. He, W. Geng, B. Zhang, L. Jia, L. Duan and Q. Zhang, *RSC Adv.*, 2016, **6**, 38391–38398.
11 K. K. Jaiswal, D. Manikandan, R. Murugan and A. P. Ramaswamy, *Eur. Polym. J.*, 2018, **98**, 177–190.
12 B. C. Yadav, S. Sikarwar, R. Yadav, P. Chaudhary, G. I. Dzhardimalieva and N. D. Golubeva, *J. Mater. Sci.: Mater. Electron.*, 2018, **29**, 7770–7777.
13 P. Chaudhary, D. K. Maurya, S. Sikarwar, B. C. Yadav, G. I. Dzhardimalieva and R. Prakash, *Eur. Polym. J.*, 2019, **112**, 161–169.
14 S. Schlecht, C. Erk and M. Yosef, *Inorg. Chem.*, 2006, **45**, 1693–1697.
15 D. Suksongkarm, S. Rojananan and S. Rojananan, *Adv. Mater. Res.*, 2013, **802**, 179–183.
16 H.-J. Gau, J.-L. Yu, C.-C. Wu, Y.-K. Kuo and C.-H. Ho, *J. Alloys Compd.*, 2009, **480**, 73–75.
17 A. Klopotov, Y. Ivanov, V. Vlasov, N. Dedov and O. Loskutov, *AIP Conf. Proc.*, 2016, **1698**, 030004.
18 S. Praiphruk, G. Lothongkum, E. Nisaratanaporn and B. Lohwongwatana, *Materialprufung*, 2013, **55**, 819–823.
19 H. M. Rawson, J. E. Begg and R. G. Woodward, *Planta*, 1977, **134**, 5–10.
20 R. B. Stringfield, *Ind. Eng. Chem.*, 1925, **17**, 833–835.
21 Z. Duan, Y. Jiang, M. Yan, S. Wang, Z. Yuan, Q. Zhao, P. Sun, G. Xie, X. Du and H. Tai, *ACS Appl. Mater. Interfaces*, 2019, **11**, 21840–21849.
22 Z. Duan, Q. Zhao, S. Wang, Z. Yuan, Y. Zhang, X. Li, Y. Wu, Y. Jiang and H. Tai, *Sens. Actuators, B*, 2020, **305**, 127534.
23 Z. Duan, Q. Zhao, S. Wang, Q. Huang, Z. Yuan, Y. Zhang, Y. Jiang and H. Tai, *Sens. Actuators, B*, 2020, **317**, 128204.
24 H. Tai, S. Wang, Z. Duan and Y. Jiang, *Sens. Actuators, B*, 2020, **318**, 128104.
25 Z. Duan, Y. Jiang, Q. Zhao, S. Wang, Z. Yuan, Y. Zhang, B. Liu and H. Tai, *Nanotechnology*, 2020, **31**, 355501.
26 S. Kiruthika, S. Singh and G. U. Kulkarni, *RSC Adv.*, 2016, **6**, 44668–44672.
27 B. Ouyang, K. Zhang and Y. Yang, *iScience*, 2018, **1**, 16–23.
28 R. K. Tripathi, O. S. Panwar, A. K. Kesarwani, I. Rawal, B. P. Singh, M. K. Dalai and S. Chockalingam, *RSC Adv.*, 2014, **4**, 54388–54397.
29 R. K. Tripathi, O. S. Panwar, I. Rawal, B. P. Singh and B. C. Yadav, *J. Taiwan Inst. Chem. Eng.*, 2018, **86**, 185–191.
30 M. Peng, X. Zheng, Z. Ma, H. Chen, S. Liu, Y. He and M. Li, *Sens. Actuators, B*, 2018, **256**, 367–373.
31 S. W. James and R. P. Tatam, *Meas. Sci. Technol.*, 2003, **14**, R49–R61.
32 W. Li, J. Liu, C. Ding, G. Bai, J. Xu, Q. Ren and J. Li, *Sensors*, 2017, **17**, 2392.
33 A. Lopez Aldaba, D. Lopez-Torres, C. Elosua, J. L. Auguste, R. Jamier, P. Roy, F. J. Arregui and M. Lopez-Amo, *Sens. Actuators, B*, 2018, **257**, 189–199.
34 M. Parthibavarman, V. Hariharan and C. Sekar, *Mater. Sci. Eng., C*, 2011, **31**, 840–844.
35 L. Xia, L. Li, W. Li, T. Kou and D. Liu, *Sens. Actuators, A*, 2013, **190**, 1–5.
36 W. Xie, M. Yang, Y. Cheng, D. Li, Y. Zhang and Z. Zhuang, *Opt. Fiber Technol.*, 2014, **20**, 314–319.
37 S. F. A. Z. Yusoff, C. S. Lim, S. R. Azzuhri, H. Ahmad and R. Zakaria, *Results Phys.*, 2018, **10**, 308–316.
38 D. Zhang, Y. E. Sun, P. Li and Y. Zhang, *ACS Appl. Mater. Interfaces*, 2016, **8**, 14142–14149.
39 L. Alwis, T. Sun and K. T. V. Grattan, *Sens. Actuators, B*, 2013, **178**, 694–699.
40 J. N. Mbithi, V. S. Springthorpe and S. A. Sattar, *Appl. Environ. Microbiol.*, 1991, **57**, 1394–1399.
41 S. Sikarwar, B. C. Yadav, S. Singh, G. I. Dzhardimalieva, S. I. Pomogailo, N. D. Golubeva and A. D. Pomogailo, *Sens. Actuators, B*, 2016, **232**, 283–291.
42 B. C. Yadav, R. C. Yadav, S. Singh, P. K. Dwivedi, H. Ryu and S. Kang, *Opt. Laser Technol.*, 2013, **49**, 68–74.
43 H. J. Naghash and O. Okay, *J. Appl. Polym. Sci.*, 1996, **60**, 971–979.
44 A. K. Solarajan, V. Murugadoss and S. Angaiah, *Sci. Rep.*, 2017, **7**, 45390.
45 K. B. Girma, V. Lorenz, S. Blaurock and F. T. Edelmann, *Z. Anorg. Allg. Chem.*, 2005, **631**, 1843–1848.
46 P. Zhang, T. Song, T. Wang and H. Zeng, *Appl. Catal., B*, 2017, **206**, 328–335.
47 N. Li, S. Liao, Y. Sun, H. W. Song and C. X. Wang, *J. Mater. Chem. A*, 2015, **3**, 5820–5828.
48 G. Vijayaprasath, R. Murugan, Y. Hayakawa and G. Ravi, *J. Lumin.*, 2016, **178**, 375–383.
49 S. Yadav, P. Chaudhary, K. Uttam, A. Varma, M. Vashistha and B. Yadav, *Nanotechnology*, 2019, **30**, 295501.
50 C. Chen, H. Qiao, S. Lin, C. Man Luk, Y. Liu, Z. Xu, J. Song, Y. Xue, D. Li, J. Yuan, W. Yu, C. Pan, S. Ping Lau and Q. Bao, *Sci. Rep.*, 2015, **5**, 11830.
51 J. Cao, Z. Wang, X. Zhan, Q. Wang, M. Safdar, Y. Wang and J. He, *Nanotechnology*, 2014, **25**, 105705.
52 A. S. Pawbake, R. G. Waykar, D. J. Late and S. R. Jadkar, *ACS Appl. Mater. Interfaces*, 2016, **8**, 3359–3365.
53 M. B. Erande, M. S. Pawar and D. J. Late, *ACS Appl. Mater. Interfaces*, 2016, **8**, 11548–11556.

54 M. S. Pawar, P. K. Bankar, M. A. More and D. J. Late, *RSC Adv.*, 2015, **5**, 88796–88804.
55 H. Bi, K. Yin, X. Xie, J. Ji, S. Wan, L. Sun, M. Terrones and M. S. Dresselhaus, *Sci. Rep.*, 2013, **3**, 2714.
56 A. Tripathy, S. Pramanik, J. Cho, J. Santhosh and A. N. Abu Osman, *Sensors*, 2014, **14**, 16343–16422.
57 Y. Wang, S. Park, J. T. W. Yeow, A. Langner and F. Müller, *Sens. Actuators, B*, 2010, **149**, 136–142.
58 H. M. J. Al-Ta'ii, Y. M. Amin and V. Periasamy, *Sci. Rep.*, 2016, **6**, 25519.
59 J. Boudaden, M. Steinmaßl, H.-E. Endres, A. Drost, I. Eisele, C. Kutter and P. Müller-Buschbaum, *Sensors*, 2018, **18**, 1516.
60 C.-Y. Lee and G.-B. Lee, *Sens. Lett.*, 2005, **3**, 1–15.
61 P.-G. Su and W.-Y. Tsai, *Sens. Actuators, B*, 2004, **100**, 417–422.
62 J. Wang, Q. Lin, R. Zhou and B. Xu, *Sens. Actuators, B*, 2002, **81**, 248–253.
63 Z. Duan, M. Xu, T. Li, Y. Zhang and H. Zou, *Sens. Actuators, B*, 2018, **258**, 527–534.
64 S. Dinc Zor and H. Cankurtaran, *J. Sens.*, 2016, **2016**, 5479092.